CrystEngComm

Facet stability of GaN during tri-halide vapor phase epitaxy: an ab initio-based approach

Journal:	*CrystEngComm*
Manuscript ID	CE-ART-11-2020-001683.R1
Article Type:	Paper
Date Submitted by the Author:	18-Dec-2020
Complete List of Authors:	Yosho, Daichi; Kyushu University, Matsuo, Yuriko; Kyushu University Research Institute for Applied Mechanics Kusaba, Akira; Kyushu University Research Institute for Applied Mechanics Kempisty, Pawel; Institute of High Pressure Physics Unipress PAS, ; Kyushu University Research Institute for Applied Mechanics, Kangawa, Yoshihiro; Kyushu University Research Institute for Applied Mechanics; Institute of Materials and Systems for Sustainability Murakami, Hisashi; Tokyo University of Agriculture and Technology Koukitu, Akinori; Tokyo University of Agriculture and Technology

SCHOLARONE™
Manuscripts

Facet stability of GaN during tri-halide vapor phase epitaxy: an ab initio-*based approach*

D. Yosho[1, a)], Y. Matsuo[2], A. Kusaba[2], P. Kempisty[2, 3], Y. Kangawa[1, 2, 4],
H. Murakami[5], A. Koukitu[5]

[1]*Department of Aeronautics and Astronautics, Kyushu University, Fukuoka 816-8580, Japan*

[2]*Research Institute for Applied Mechanics, Kyushu University, Fukuoka 816-8580, Japan*

[3]*Institute of High Pressure Physics, Polish Academy of Sciences, Sokolowska 29/37, 01-142 Warsaw, Poland*

[4]*Institute of Materials and Systems for Sustainability, Nagoya University, Nagoya 464-8601, Japan*

[5]*Department of Applied Chemistry, Tokyo University of Agriculture and Technology, Tokyo 184-8588, Japan*

a) yosho@riam.kyushu-u.ac.jp

An ab initio-based approach is used to investigate the facet stability of GaN during tri-halide vapor phase epitaxy (THVPE). First, surface reconstructions are analyzed to create surface phase diagrams as a function of the gaseous pressure and temperature. Next, a triangular wedge model is used to compute absolute surface formation energies with the bulk state as a reference. A Wulff construction is used to predict the crystal growth form composed of energetically preferred facets. The calculated results can be used to control the shape of GaN grown by THVPE.

INTRODUCTION

Gallium nitride (GaN) is an attractive material for optics and high-power electronics applications because of excellent physical properties, such as a direct wide band gap, high electron mobility and high thermal conductivity.[1-6] Several methods are used to manufacture GaN crystals, such as metal-organic vapor phase epitaxy (MOVPE) and halide vapor phase epitaxy (HVPE).[7, 8] Among these methods, HVPE produces bulk crystals or self-standing substrates with a superior growth rate and crystalline quality.[9] Recently, tri-halide vapor phase epitaxy (THVPE), in which $GaCl_3$ replaces GaCl as a Ga source, has been developed to fabricate bulk GaN.[10-12] The higher driving force for deposition in THVPE than in HVPE results in a higher GaN growth rate.[11] This larger driving force for deposition allows to increase the growth temperature, resulting in superior crystal quality.[11, 12] Therefore, THVPE is an interesting alternative to HVPE because of the advantages of a high growth rate and a high growth temperature.

Facet control during growth using the epitaxial lateral overgrowth technique is known to be crucial for reducing the threading dislocation density.[13, 14] Facet formation of a buffer layer has also been controlled to improve the optical properties of an InGaN light emitting diode constructed on the buffer layer.[15] From both scientific and technical viewpoints: the

crystallography, the underlying principles controlling the growth form, and the fundamental mechanism for GaN epitaxy, it is important to investigate naturally emerging polar, semipolar and nonpolar planes during growth. GaN crystallizes in the non-centrosymmetric hexagonal structure of the wurtzite (space group P63mc), where the [0001] and [000-1] crystallographic directions are not equivalent. In this paper, 4-index notation *hkil*, called as Miller-Bravais notation, will be used to denote crystal directions and planes. In 2017, Iso et al.[16] used the selected area growth (SAG) of the nonpolar m-plane (10–10) and the polar –c-plane (000–1) of GaN to determine the growth form and the quasi-equilibrium crystal shape (quasi-ECS) under THVPE. Experimental observations showed that the polar N-face (000–1) and the nonpolar m-plane {10–10} were consistently stable at low and high temperatures, whereas semipolar planes {10–1–1} only formed at high temperature. The purpose of this study is to theoretically determine how THVPE growth conditions affect the growth form of GaN.

Many putative atomic reconstructions must be analyzed to determine the stability of each surface. Ab initio calculations are typically used to study surface reconstruction by determining the surface formation energy as a function of the chemical potential of the component elements (taken as an independent parameter). However, these theoretical construction are difficult to compare against experimental parameters of gaseous pressures and growth temperatures.[17, 18] In 2001, Kangawa et al.[19] used an ab initio-based approach based on the gas phase free energy to predict the adsorption-desorption behavior of adatoms under a prescribed gas pressure and temperature. The proposed approach could be used to relate the surface formation energy to the growth conditions.[20, 21] However, the disadvantage of the early version of this approach is that the reference to calculating the formation energy for each group of surfaces with the same crystallographic indices is their unreconstructed ideal state. The relative stability of different facets can only be compared by using absolute surface formation energies (the energy of the bulk state is used as the reference). In this study, we used a modified ab initio-based approach to analyze stable surface reconstruction on the (0001), (000−1), (10−10), (10−11), and (10−1−1) surfaces, and determined the surface phase diagram as a function of the temperature and partial pressure. Then these diagrams were used to determine the facet stability and to perform a thermodynamic analysis to serve as a database.[22] We used Wulff construction to investigate the shape of GaN crystal growing under THVPE conditions.

CALCULATION SCHEME

First, we determine stable surface reconstruction on the (0001), (000−1), (10−10), (10−11), and (10−1−1) surfaces. Surface reconstructions on GaN surfaces during HVPE and THVPE are analyzed for reference. In this study, two partial pressures are considered. The partial pressure at the inlet, p^0, is referred to as the input partial pressure, and the partial pressure at the growth section, p', is referred to as the decomposed partial pressure. The carrier gas, which may be hydrogen,

nitrogen, or a hydrogen-nitrogen mixture, transports the source gases, such as GaCl and $GaCl_3$, to the growth section. The following decomposition reactions occur near the substrate during HVPE:

$$GaCl(g) \rightarrow Ga(g) + \frac{1}{2}Cl_2(g), \quad (1)$$

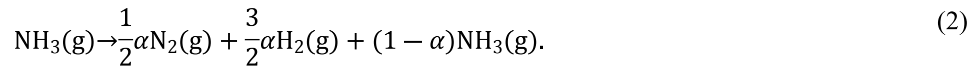

$$NH_3(g) \rightarrow \frac{1}{2}\alpha N_2(g) + \frac{3}{2}\alpha H_2(g) + (1-\alpha)NH_3(g). \quad (2)$$

Here, α is the decomposition ratio of ammonia and is set to 0.25 in accordance with a previous study.[22, 23] p^0 is solely determined using the ratio of the molar flow rates and the total pressure. p' is determined by the molar ratios corresponding to the chemical reactions given in Eqs. (1) and (2) and is expressed as

$$p'_{Ga} = c \cdot p^0_{GaCl}, \quad (3)$$

$$p'_{NH3} = c \cdot (1-\alpha)p^0_{NH3}, \quad (4)$$

$$p'_{N2} = c \cdot \left[p^0_{N2} + \frac{1}{2}\alpha p^0_{NH3}\right], \quad (5)$$

$$p'_{H2} = c \cdot \left[p^0_{H2} + \frac{3}{2}\alpha p^0_{NH3}\right], \quad (6)$$

$$p'_{Cl2} = c \cdot \frac{1}{2}p^0_{GaCl}, \quad (7)$$

where c is a normalization constant used to maintain the total pressure. p' is an input variable used to determine the surface phase diagram, although p^0 is shown for the calculation condition given below. To model THVPE, Eq. (2) and Eqs. (4)-(6) are used, as for HVPE; however, Eq. (1) is replaced by

$$GaCl_3(g) \rightarrow Ga(g) + \frac{3}{2}Cl_2(g), \quad (8)$$

Eq. (3) is replaced by

$$p'_{Ga} = c \cdot p^0_{GaCl3}, \quad (9)$$

and Eq. (7) is replaced by

$$p'_{\mathrm{Cl2}} = c \cdot \frac{3}{2} p^{0}_{\mathrm{GaCl3}}. \tag{10}$$

Within the approach formulated by Kangawa et al.,[19-21] the surface with the lowest formation energy appears at equilibrium. The surface formation energy based on an unreconstructed ideal structure without adsorbates is written as

$$E_{\mathrm{f}} = E^{\mathrm{recon}}_{\mathrm{surface}} - E^{\mathrm{ideal}}_{\mathrm{surface}} - n^{\mathrm{ad}}_{\mathrm{Ga}}\left(E^{\mathrm{gas}}_{\mathrm{Ga}} + \mu^{\mathrm{gas}}_{\mathrm{Ga}}\right) - \frac{1}{2}\left\{n^{\mathrm{ad}}_{\mathrm{N}}\left(E^{\mathrm{gas}}_{\mathrm{N2}} + \mu^{\mathrm{gas}}_{\mathrm{N2}}\right) + n^{\mathrm{ad}}_{\mathrm{H}}\left(E^{\mathrm{gas}}_{\mathrm{H2}} + \mu^{\mathrm{gas}}_{\mathrm{H2}}\right) + n^{\mathrm{ad}}_{\mathrm{Cl}}\left(E^{\mathrm{gas}}_{\mathrm{Cl2}} + \mu^{\mathrm{gas}}_{\mathrm{Cl2}}\right)\right\}, \tag{11}$$

where $E^{\mathrm{recon}}_{\mathrm{surface}}$and $E^{\mathrm{ideal}}_{\mathrm{surface}}$ are the total energies at absolute zero of the reconstructed and ideal surface systems, respectively; $E^{\mathrm{gas}}_{\mathrm{Ga}}$, $E^{\mathrm{gas}}_{\mathrm{N2}}$, $E^{\mathrm{gas}}_{\mathrm{H2}}$, and $E^{\mathrm{gas}}_{\mathrm{Cl2}}$ are the total energies at absolute zero of the Ga, N_2, H_2, and Cl_2 molecules, respectively; $\mu^{\mathrm{gas}}_{\mathrm{Ga}}$, $\mu^{\mathrm{gas}}_{\mathrm{N2}}$, $\mu^{\mathrm{gas}}_{\mathrm{H2}}$, and $\mu^{\mathrm{gas}}_{\mathrm{Cl2}}$ are the chemical potentials at the growth temperatures and partial pressures of the Ga, N_2, H_2, and Cl_2 molecules, respectively; and $n^{\mathrm{ad}}_{\mathrm{Ga}}$, $n^{\mathrm{ad}}_{\mathrm{N}}$, $n^{\mathrm{ad}}_{\mathrm{H}}$, and $n^{\mathrm{ad}}_{\mathrm{Cl}}$ are the numbers of Ga, N, H, and Cl adatoms on the reconstructed surface, respectively. The chemical potential of a gas molecule is expressed as a function of the temperature T and partial pressure p as follows:

$$\mu = -k_B T \ln\left(\frac{g k_B T}{p} \times \zeta_{\mathrm{trans}} \zeta_{\mathrm{rot}} \zeta_{\mathrm{vibr}}\right), \tag{12}$$

$$\zeta_{\mathrm{trans}} = \left(\frac{2\pi m k_B T}{h^2}\right)^{\frac{3}{2}}, \tag{13}$$

$$\zeta_{\mathrm{rot}} = \frac{1}{\pi\sigma}\left[\frac{8\pi^3 (I_A I_B \cdots)^{\frac{1}{n}} k_B T}{h^2}\right]^{\frac{n}{2}}, \tag{14}$$

$$\zeta_{\mathrm{vibr}} = \prod_{i}^{3N-3-n}\left[1 - \exp\left(-\frac{h\upsilon_i}{k_B T}\right)\right]^{-1}, \tag{15}$$

where ζ_{trans}, ζ_{rot}, and ζ_{vibr} are the partition functions for translational, rotational, and vibrational motion, respectively. k_B is Boltzmann's constant, h is Planck's constant, g is the degree of degeneracy of the electron energy level, m is the mass of one particle, n is the rotational degree of freedom, σ is the symmetry factor, I_I is the moment of inertia, i is the vibrational degree of freedom, N is the number of atoms in the respective particle, and ν is the frequency. Thus, Eqs. (11)-(15) describe the surface formation energy as a function of the temperature and partial pressure.

The total energies were calculated by the DMol[3] software package[24, 25] based on density functional theory (DFT) with the Perdew–Burke–Ernzerhof (PBE) functional[26] and the double numerical plus polarization (DNP) basis set. The surface slab model comprised a vacuum layer more than 20 Å thick and five GaN bilayers, with a fixed bottom layer that was passivated with fictitious hydrogen atoms[27]. A basis set cutoff of 4.8 Å and a 3 × 3 × 1 Monkhorst–Pack (MP) *k*-point mesh[28] were used to create (2 × 2) surface slab models of (0001), (000−1), and (10−10) GaN and (1 × 2) surface slab models of (10−11), and (10−1−1) GaN. Geometry optimization convergence thresholds of 2.0×10^{-5} Ha, 0.0005 Ha/Å, and 0.005 Å were used for the energy change, maximum force, and maximum displacement, respectively. These calculation conditions were the same as those used in previous studies by our group.[22, 29, 30] Fig. 1 is a schematic of atomic configurations for the reconstructed surface that appears in the phase diagram (Fig. 2). A sufficient number of candidates other than those shown in Fig. 1 were considered in this study. These atomic configurations were chosen based on the literature[22, 29, 31-33] and the electron counting (EC) rule[34]: that is, an electronically passivated surface is energetically favorable for the system. Eq. (11) was used to determine the surface with the lowest formation energy among the considered surfaces under the prescribed growth condition.

Second, we determined the absolute surface formation energy. This energy can be calculated using the following formula:

$$E_{\mathrm{f}}^{\mathrm{recon\leftarrow bulk}} = E_{\mathrm{f}} + E_{\mathrm{f}}^{\mathrm{ideal\leftarrow bulk}}, \tag{16}$$

where E_{f} is the surface formation energy of each structure calculated by Eq. (11), and $E_{\mathrm{f}}^{\mathrm{ideal\leftarrow bulk}}$ is the surface formation energy of the ideal structure based on the bulk state. $E_{\mathrm{f}}^{\mathrm{ideal\leftarrow bulk}}$ is written as

$$E_{\mathrm{f}}^{\mathrm{ideal\leftarrow bulk}} = E_{\mathrm{surface}}^{\mathrm{ideal}} - n_{\mathrm{GaN}}\mu_{\mathrm{GaN}} - A_{\mathrm{slab}}\sigma_{\mathrm{pass}}, \tag{17}$$

where n_{GaN} is the number of GaN pairs in the slab model, μ_{GaN} is the chemical potential of GaN (bulk), A_{slab} is the surface area of the slab model, and σ_{pass} is the passivated surface energy per unit area. Note that $E_{\mathrm{f}}^{\mathrm{recon\leftarrow bulk}}$, E_{f}, $E_{\mathrm{f}}^{\mathrm{ideal\leftarrow bulk}}$, and $E_{\mathrm{surface}}^{\mathrm{ideal}}$ are determined for the (2 × 2) surface for the (0001), (000−1), and (10−10) surfaces and for the (1 × 2) surface for (10−11) and (10−1−1) surfaces. σ_{pass} is calculated by the triangular wedge model, and the detailed calculation procedures can be found in the literature.[22, 31, 35, 36] Indeterminate energies are obtained using the triangular wedge model, because the Ga and N chemical potentials are obtained using $\mu_{\mathrm{Ga}} + \mu_{\mathrm{N}} = \mu_{\mathrm{GaN}}$. This relationship is used as an equilibrium condition, and the

absolute surface formation energy is estimated as a function of μ_{Ga} or μ_{N}, which can vary over the thermodynamically allowed range $\mu_{\mathrm{Ga}}(bulk) \geq \mu_{\mathrm{Ga}} \geq \mu_{\mathrm{Ga}}(bulk) + \Delta H_f(GaN)$, where ΔH_f is the GaN formation enthalpy and $\mu_{\mathrm{Ga}}(bulk)$ is the chemical potential of bulk Ga.[20, 21, 37-40] A maximum in μ_{Ga} is called a Ga-rich condition, and a minimum in μ_{Ga} is called an N-rich condition.

Finally, we use Wulff's theorem to determine how the gas phase affects the equilibrium shape or facet emergence and explain experimental THVPE results. Details of the equilibrium Wulff construction are explained elsewhere.[41-44]

RESULTS AND DISCUSSION

Fig. 2 shows the surface phase diagram corresponding to the most stable surface reconstruction as a function of the temperature and the V/III ratio. For HVPE growth under the growth condition (T = 1050 ℃ and V/III = 50) using H_2 or N_2 carrier gases, 3Ga-Cl, 3N-H, 4N-H+4Ga-Cl, 2N-H2+5N-H, and 8Ga-Cl structures appear for (000−1), (0001), (10−10), (10−11), and (10−1−1) growth, respectively. For THVPE growth under the growth condition (T = 1230 ℃ and V/III = 50) using an N_2 carrier gas, 3Ga-Cl, 3N-H, ideal, 2N-H2+5N-H, and ideal structures appear for (000−1), (0001), (10−10), (10−11), and (10−1−1) growth, respectively. The reconstructed structures appearing in Fig. 2 typically satisfy the EC rule, e.g., 3Ga-Cl for the (0001) surface. The EC rule is also satisfied by 3Ga-H for the (0001) surface and that structure appears under MOVPE conditions.[19] However, 3Ga-Cl, and not 3Ga-H, appears under HVPE conditions. This result suggests that the Ga-Cl bond is stronger than the Ga-H bond. However, the N-H bond is stronger than the N-Cl bond, because the 3N-H structure appears even though 3N-Cl also satisfies the EC rule for the (000−1) surface.[45] The 4N-H+4Ga-Cl, 2N-H2+5N-H, and 8Cl appear for the (10−10), (10−11), and (10−1−1) surfaces, because the Ga-Cl and N-H bonds are strong. The ideal structure appears at high temperature for the (10−10) and (10−1−1) surfaces, because the chemical potential of molecules, such as H_2 and Cl_2, decrease as the temperature increases (see Eq. (12)), and these molecules are more stable in the gas phase than on the aforementioned surfaces.

We discuss the quasi-ECS during THVPE growth. The same reconstructed structure appears for the (0001), (000−1), and (10−11) surfaces at both 1050 ℃ and 1230 ℃. This structure changes at 1050 ℃ and 1230 ℃ for the (10−10) and (10−1−1) surfaces. This surface phase change influences the quasi-ECS. Fig. 3 shows the absolute surface formation energy of the reconstructed surface under THVPE experimental conditions (T = 1050 ℃ and 1230 ℃). The energies vary within the thermodynamically allowed range, and physical phenomena occur at one point within this range. Since the local partial pressures of the active gases in the experiment are not known exactly (these are parameters strongly dependent on the

geometry of the reactor), the chemical potential has to be linked to the actual growth condition by estimation. In general, it is useful to perform CFD simulations to obtain local concentrations of species in the growth zone and directly above the substrate crystal. Despite all this, our investigation showed that the calculated results and experimental results are in good agreement when N-rich conditions are adopted in our model. Thus, we present our interpretation of the thermodynamic reasons for the crystal shape observed in the experiments assuming N-rich conditions growth mode.[16] The (000−1) and (10−10) surfaces emerged at both 1050 °C and 1230 °C in the experiment,[16] because these surfaces have a lower absolute surface formation energy than other possible surfaces. Stable faceted surfaces tend to emerge during quasi-equilibrium growth. Emergence of the (0001) surface was not experimentally observed at any temperature, because this surface has a high absolute surface formation energy. Although emergence of the {10–1–1} surface was experimentally observed at high temperature,[16] the {10–11} surface did not emerge at any temperature. This result is consistent with our calculations as (10–11) surface has a higher absolute surface formation energy than (10–1–1). Fig. 4 is a schematic of the Wulff construction and the quasi-ECS at 1050 °C and 1230 °C. The upper part of Fig. 4 is a 2D schematic of the absolute surface formation energy for various orientations. Here, O is the origin point, that is, the Wulff point, and P, Q, and R are determined from the absolute surface formation energies for the (000−1), (10−10), and (10−1−1) surfaces respectively. The angle θ denotes the surface orientation of GaN. The lower part of Fig. 4 shows the quasi-ECS based on the Wulff construction. The shape agrees with experimental results,[16] confirming the feasibility of our calculation. The absolute surface formation energy of the (000−1) and (10−10) surfaces is 0.080 eV/Å2 and 0.066 eV, respectively, at 1050 ℃ and 0.10 eV/$Å^2$ and 0.11 eV/$Å^2$, respectively, at 1230 ℃. This destabilization of the (000−1) and (10−10) surfaces explains why the emergence of the {10–1−1} surface was only experimentally observed at 1230 ℃.[16] Further quantitative refinements to the theoretical model can be made taking into account the contribution of thermal vibrations of surface atoms.[46] However, as mentioned, it is essential to obtain precise information on the local conditions (temperature and partial pressure) in experimental systems in the immediate vicinity of the growing crystal.

CONCLUSIONS

In conclusion, we performed ab initio calculations to elucidate the facet emergence mechanism during THVPE-SAG. First, we analyzed the stable reconstruction of (0001), (000−1), (10−10), (10−11), and (10−1−1) surfaces during GaN growth and determined the surface phase diagram as a function of the temperature and partial pressure. Then, we calculated the absolute surface formation energy using the bulk state as a reference. We used the absolute surface formation energy and Wulff construction to describe the facet emergence mechanism during THVPE-SAG in terms of surface stability. The

predicted facets emerging during SAG are consistent with reported experimental observations. The results of the present study can help understand surface phenomena during GaN growth and to obtain high-quality GaN crystals using HVPE and THVPE.

FIGURES

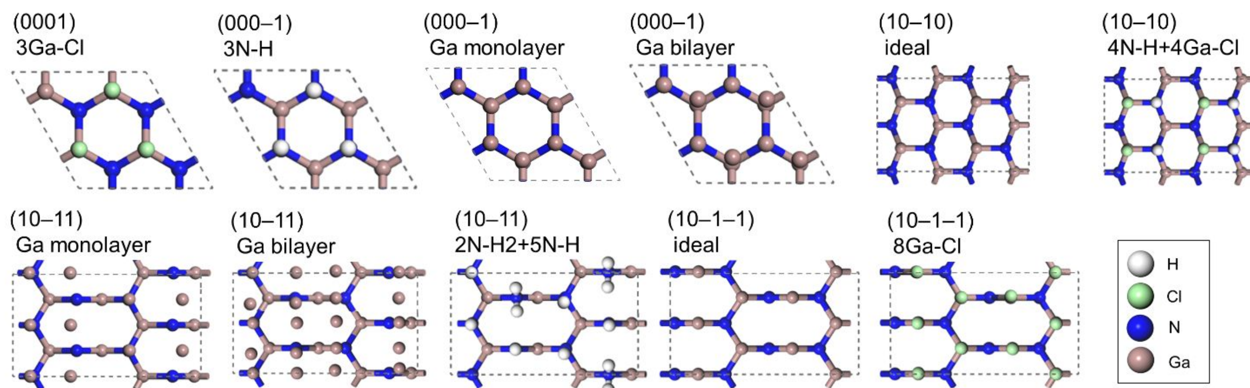

FIG. 1. Candidate reconstructed structures that appear in surface phase diagram: dashed lines indicate (2×2) unit cells for (0001), (000−1), and (10−10) and (1×2) unit cells for (10−11) and (10−1−1)

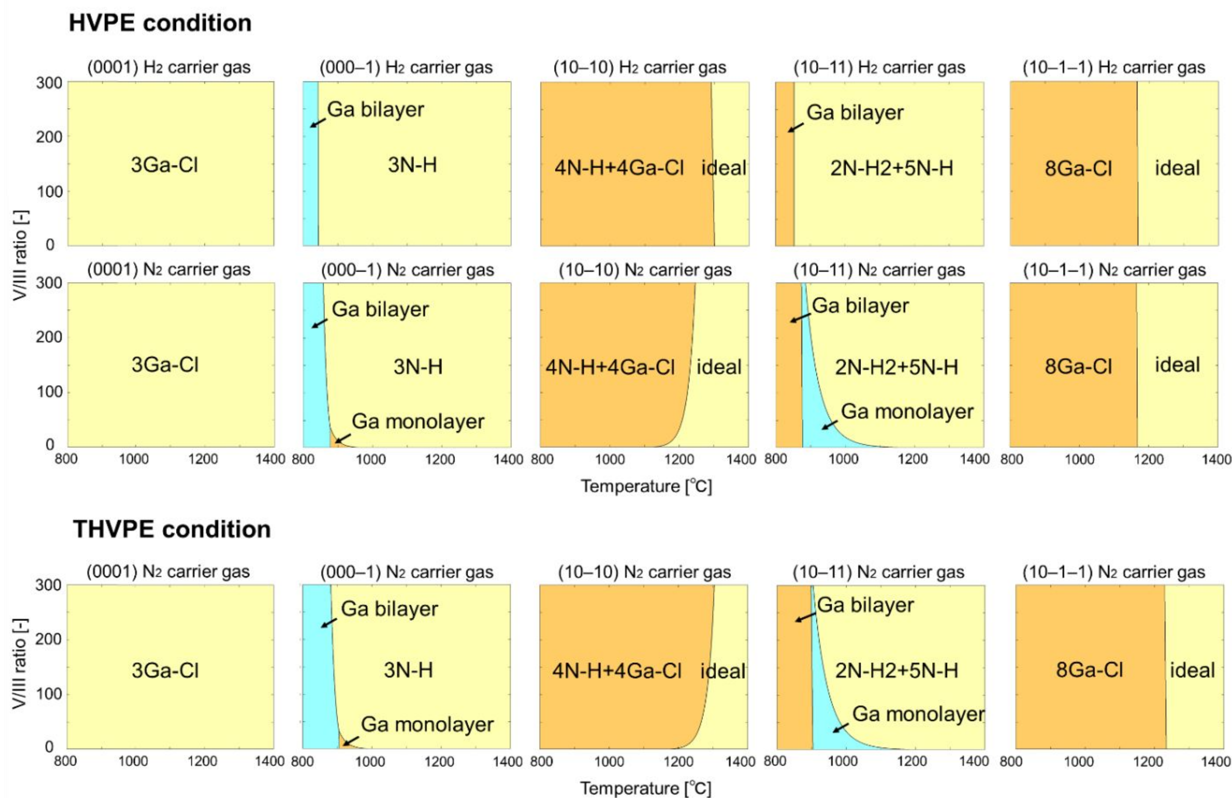

FIG. 2. Surface phase diagram for (0001), (000−1), (10−10), (10−11), and (10−1−1): $p^0{}_{\mathrm{GaCl}} = 1.1 \times 10^{-3}$ atm and $\alpha = 0.25$ under HVPE conditions; $p^0{}_{\mathrm{GaCl3}} = 2.2 \times 10^{-3}$ atm and $\alpha = 0.25$ under THVPE conditions; total pressure is 1 atm for all growth conditions

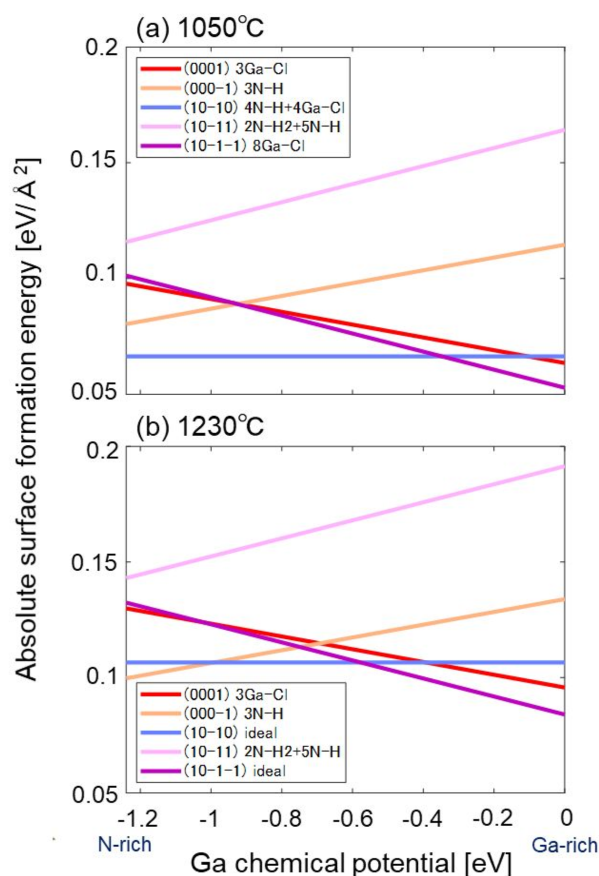

FIG. 3. Absolute surface formation energies of several GaN surfaces that can occur during THVPE at (a) 1050 ℃ and (b) 1230 ℃ as a function of a wide range of Ga chemical potential changes, showing that the typical THVPE experiments discussed in this paper were carried out under N-rich conditions, i.e., the Ga chemical potential is close to the value on the left side of the graph

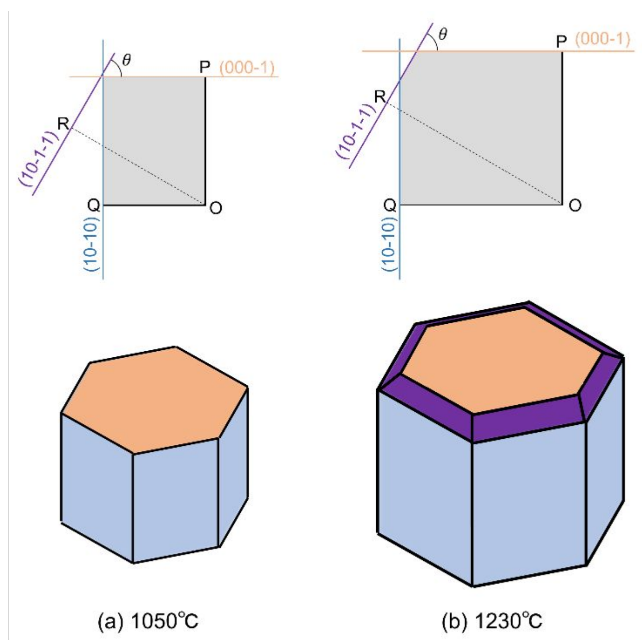

FIG. 4. Schematic 2D Wulff construction and equilibrium morphology change during THVPE for growth temperatures of (a) 1050 ℃ and (b) 1230 ℃. O is the origin point, that is, the Wulff point, and P, Q, and R are determined from the absolute surface formation energies for the (000−1), (10−10), and (10−1−1) surfaces respectively.

ACKNOWLEDGMENTS

This study was partially supported by JST A-STEP (AS2915123T), JSPS KAKENHI (Grant Number JP16H06418), the National Science Centre of Poland (Grant Number 2017/27/B/ST3/01899) and the MEXT "Program for Research and Development of Next-Generation Semiconductors to Realize an Energy-Saving Society (Grant Number JPJ005357)".

REFERENCES

1. H. Amano et al., Journal of Physics D: Applied Physics **51**, 163001 (2018).
2. K. Shojiki, T. Tanikawa, J.-H. Choi, S. Kuboya, T. Hanada, R. Katayama, and T. Matsuoka, Applied Physics Express **8**, 061005 (2015).
3. A. Tanaka, W. Choi, R. Chen, and S. A. Dayeh, Advanced Materials **29**, 1702557 (2017).
4. Y. Zhang, A. Dadgar, and T. Palacios, Journal of Physics D: Applied Physics **51**, 273001 (2018).
5. T. Kachi, Japanese Journal of Applied Physics **53**, 100210 (2014).
6. C. Gupta, Y. Enatsu, G. Gupta, S. Keller, and U. K. Mishra, Physica Status Solidi A **213**, 878 (2016).
7. K. Hiramatsu, S. Itoh, H. Amano, I. Akasaki, N. Kuwano, T. Shiraishi, and K. Oki, Journal of Crystal Growth **115**, 628 (1991).
8. K. Naniwae, S. Itoh, H. Amano, K. Itoh, K. Hiramatsu, and I. Akasaki, Journal of Crystal Growth **99**, 381 (1990).
9. H. Fujikura, T. Konno, T. Yoshida, and F. Horikiri, Japanese Journal of Applied Physics **56**, 085503 (2017).
10. T. Yamane, K. Hanaoka, H. Murakami, Y. Kumagai, and A. Koukitu, Physica Status Solidi C **8**, 1471 (2011).
11. H. Murakami, N. Takekawa, A. Shiono, Q. T. Thieu, R. Togashi, Y. Kumagai, K. Matsumoto, and A. Koukitu, Journal of Crystal Growth **456**, 140 (2016).
12. T. Hirasaki, K. Asano, M. Banno, M. Ishikawa, F. Sakuma, H. Murakami, Y. Kumagai, A. Koukitu, Japanese Journal of Applied Physics **53**,05FL02 (2014).
13. A. Usui, H. Sunakawa, A. Sakai, A. A. Yamaguchi, Japanese Journal of Applied Physics **36**, L899 (1997).
14. A. Sakai, Applied Physics Letters **71**, 2259 (1997).
15. A. Sakaki, M. Funato, M. Miyano, T. Okazaki, Y. Kawakami, Scientific Reports **9**, 3733 (2019).
16. K. Iso, K. Matsuda, N. Takekawa, H. Murakami, and A. Koukitu, Physica Status Solidi B **254**, 1600679 (2017).
17. J. E. Northrup, Physical Review B: Condensed Matter **44**, 1419 (1991).

18. A. R. Smith, R. M. Feenstra, D. W. Greve, J. Neugebauer, and J. E. Northrup, Physical Review Letters **79**, 3934 (1997).

19. Y. Kangawa, T. Ito, A. Taguchi, K. Shiraishi, and T. Ohachi, Surface Science **493**, 178 (2001).

20. Y. Kangawa, T. Akiyama, T. Ito, K. Shiraishi, and T. Nakayama, Materials (Basel) **6**, 3309 (2013).

21. T. Matsuoka, Y. Kangawa (eds.), Epitaxial Growth of III-Nitride Compounds: Computational Approach, Springer Series in Materials Science, **269** (2018).

22. A. Kusaba, Y. Kangawa, P. Kempisty, H. Valencia, K. Shiraishi, Y. Kumagai, K. Kakimoto, and A. Koukitu, Japanese Journal of Applied Physics **56**, 070304 (2017).

23. Y. Inatomi, Y. Kangawa, K. Kakimoto, and A. Koukitu, Japanese Journal of Applied Physics **56**, 038002 (2017).

24. B. Delley, Journal of Chemical Physics **92**, 508 (1990).

25. B. Delley, Journal of Chemical Physics **113**, 7756 (2000).

26. J. P. Perdew, K. Burke, and M. Ernzerhof, Physical Review Letters **77**, 3865 (1996).

27. K. Shiraishi, Journal of the Physical Society of Japan **59**, 3455 (1990).

28. H. J. Monkhorst and J. D. Pack, Physical Review B **13**, 5188 (1976)

29. Y. Inatomi and Y. Kangawa, Applied Surface Science **502**, 144205 (2020).

30. D. Yosho, Y. Inatomi, and Y. Kangawa, Japanese Journal of Applied Physics **59**, 048002 (2020).

31. Y. Seta, T. Akiyama, A. M. Pradipto, K. Nakamura, and T. Ito, Journal of Crystal Growth **510**, 7 (2019).

32. Y. Seta, A. M. Pradipto, T. Akiyama, K. Nakamura, T. Ito, A. Kusaba, and Y. Kangawa, Japanese Journal of Applied Physics **58**, Sc1014 (2019).

33. T. Yayama, Y. Kangawa, and K. Kakimoto, Japanese Journal of Applied Physics **52**, 08JC02 (2013).

34. M. D. Pashley, Physical Review B: Condensed Matter **40**, 10481 (1989).

35. S. B. Zhang and S. H. Wei, Physical Review Letters **92**, 086102 (2004).

36. C. E. Dreyer, A. Janotti, and C. G. Van de Walle, Physical Review B **89**, 081305 (2014).

37. T. Akiyama, T. Yamashita, K. Nakamura, and T. Ito, Japanese Journal of Applied Physics **48**, 120218 (2009).

38. T. Akiyama, T. Yamashita, K. Nakamura, and T. Ito, Japanese Journal of Applied Physics **49**, 030212 (2010).

39. T. Akiyama, D. Ammi, K. Nakamura, and T. Ito, Physical Review B **81**, 245317 (2010).

40. T. Akiyama, T. Yamashita, K. Nakamura, and T. Ito, Journal of Crystal Growth **318**, 79 (2011).

41. G. Wulff, Zeitschrift für Kristallographie – Crystalline Materials **34**, 449 (1901).

42. H. Li, L. Geelhaar, H. Riechert, and C. Draxl, Physical Review Letters **115**, 085503 (2015).

43. G. Barmparis, Z. Lodziana, N. Lopez, I. Remediakis, Beilstein Journal of Nanotechnology **6**, 361 (2015).

44. Y. Seta, A.-M. Pradipto, T. Akiyama, K. Nakamura, and T. Ito, Physica Status Solidi B **257**, 1900523 (2020).

45. J. E. Northrup and J. Neugebauer, Applied Physics Letters **85**, 3429 (2004).

46. P. Kempisty and Y. Kangawa, Phys. Rev. B 100, 085304 (2019).